Journal of Materials Chemistry A

ROYAL SOCIETY OF CHEMISTRY

PAPER

View Article Online
View Journal | View Issue

Cite this: J. Mater. Chem. A, 2023, 11, 4801

A novel stable zinc–oxo cluster for advanced lithography patterning†

Youming Si,[a] Yingdong Zhao,[a] Guangyue Shi,[d] Danhong Zhou,[a] Feng Luo,[d] Pengzhong Chen, *[ab] Jiangli Fan *[ac] and Xiaojun Peng [ac]

Received 6th January 2023
Accepted 6th February 2023

DOI: 10.1039/d3ta00115f

rsc.li/materials-a

Recently, the development of novel metal-containing resists has received much attention in extreme ultraviolet lithography (EUVL) owing to their smaller sizes and higher EUV absorptivity than traditional polymer resists. Herein, we report zinc (Zn)–**VBA**, a novel stable zinc–oxo cluster-based photoresist molecule with the $[Zn_4O]^{6+}$ inner core and six organic ligands based on 4-vinylbenzoic acid. Zn–**VBA** was simply prepared by the reactions between the zinc-oxide and 4-vinylbenzoic acid, exhibiting atomically precise structure and good batch stability. Based on single-crystal X-ray diffraction analysis, the size of Zn–**VBA** is 2.2 nm, which is in line with the high-resolution requirements for advanced lithography technology. Zn–**VBA** exhibits excellent thermal stability up to 400 °C, much better than the reported zinc-based clusters. Moreover, theoretical studies have revealed the roles of organic ligands in their high thermal stability. Spin-coating methods were employed to fabricate homogenous thin films of Zn–**VBA**, which showed a quite small roughness value in the absence of viscosifiers, as confirmed by atomic force microscopy images. More importantly, the Zn–**VBA** films performed well in the electron beam lithography (EBL) and EUVL tests without the addition of photoinitiators, giving prominent pattern lines. This work proves the structural advantages of benzoic-acid-based zinc–oxo clusters as promising EUV patterning materials, which inspire future exploration of metal–oxo clusters (MOCs) resist materials for advanced lithography.

Introduction

In the semiconductor industry, downscaling of device size in integrated circuits often pushes lithography technology[1,2] to its resolution limits by continuously decreasing the wavelength of the light source. Therefore, it is important to develop photoresist materials that are compatible and have an optimized response to light irradiation.[3,4] Because of EUV's ability to achieve sub-10 nm node patterns with high resolution, a commercial shift from deep ultraviolet (DUV, $\lambda = 193$ nm) lithography (DUVL) to shorter extreme ultraviolet (EUV, $\lambda = 13.5$ nm) lithography (EUVL) is underway.[5–8] This shift overturned the traditional DUV lithography. Unlike DUVL, where UV light induces photoacid generation, EUV photons (92 eV) ionize most materials encountered. The role of the electron cascade produced by photoionization is still being investigated. In addition, when compared to DUV 193 nm lithography, the photon density of EUV was reduced to only 7% at a given exposure dose, resulting in appreciable statistical fluctuation. The drastic change in the photo energy, reduced photon density, and high-resolution patterns pose challenges regarding the chemically amplified resists (CARs), which are the workhorses of the DUVL. The large size and low EUV absorptivity of polymer-based CARs have become critical points, particularly in terms of resolution. Moreover, the stochastic distribution of chemical reactions easily occurs around the photon absorption area owing to the heterogeneities in the composition of CAR film. It may result in a high defect density in the patterns. Therefore, to circumvent the challenges posed by CARs, a new class of photoresist platforms are required to be developed. The most important design criteria for optimizing photoresist performance in EUV require research on materials with high EUV absorption elements, defined molecular structures, as well as small and homogeneous sizes.[9–15]

Metal oxides[16–18] that can incorporate high EUV absorption elements into the molecular frameworks exhibit promising application prospects in EUVL. In particular, among the various metal oxides, MOCs are hybrid inorganic–organic molecular compounds with a well-defined number of metallic elements

[a]State Key Laboratory of Fine Chemicals, Frontiers Science Center for Smart Materials Oriented Chemical Engineering, School of Chemical Engineering, Dalian University of Technology, Dalian 116024, China. E-mail: fanjl@dlut.edu.cn

[b]Ningbo Institute of Dalian University of Technology, Ningbo 315016, China

[c]Research Institute of Dalian University of Technology in Shenzhen, Shenzhen 518057, China

[d]School of Materials Science and Engineering, Nankai University, Tianjin 300350, China

† Electronic supplementary information (ESI) available. CCDC 2215806 and 2225688. For ESI and crystallographic data in CIF or other electronic format see DOI: https://doi.org/10.1039/d3ta00115f

and organic ligands. It is generally assumed that the central metallic atoms are able to absorb a large fraction of the EUV light and show high etch resistance, while the peripheral organic shells are responsible for processing and solubility switching properties. When exposed to EUV radiation, such materials usually undergo loss or decomposition of organic ligands, followed by crosslinking of metal and oxygen bonds to form a metal oxide network primarily acting as negative tone photoresists. Because of the wide range of metal centers and organic ligands available, the structures and properties of MOCs are highly variable and tunable.[19,20] Among the transition metals with 3d electrons, zinc (Zn)-based MOCs have gained much attention. The absorption cross section[21] of zinc–oxo clusters for 13.5 nm EUV[22,23] is an order of magnitude higher than that of organic polymers. Moreover, zinc–oxo clusters are nontoxic and in line with the concept of green lithography.[24,25] However, because of the uncertainty in synthesis, the structures of most reported zinc–oxo clusters are not well defined, resulting in undesirable purity and batch instability. Additionally, additives, such as photoinitiators or viscosifiers, are usually needed to initiate the chemical reaction of zinc–oxo clusters and improve the film formation for the lithography process.

Herein, we report a novel zinc–oxo cluster, *i.e.*, Zn–**VBA**, containing 4-vinylbenzoic acid (**VBA**) as a component of the organic shell around the $[Zn_4O]^{6+}$ core. Compared to the reported zinc–oxo clusters, Zn–**VBA** exhibits advantages including simple preparation, good batch stability, and atomically precise structure. More importantly, Zn–**VBA** is a single-component photoresist material that is able to occur photolithographic reaction without photoinitiators. Single-crystal X-ray diffraction analysis revealed a Zn–**VBA** of 2.2 nm, which follows the high-resolution requirements for advanced resist compositions.[16,26,27] (Scheme 1). Both experimental and theoretical methods were used to systematically study the thermal stability, solubility, and film-forming capability of Zn–**VBA**. By using cyclohexanone and propylene glycol monomethyl ether acetate (PGMEA) as spin-coating solvents, Zn–**VBA** formed a uniform thin film with extremely low roughness. Moreover, in the EBL and EUVL tests, Zn–**VBA** produced prominent pattern lines, exhibiting the potential as promising patterning materials for advanced lithography.

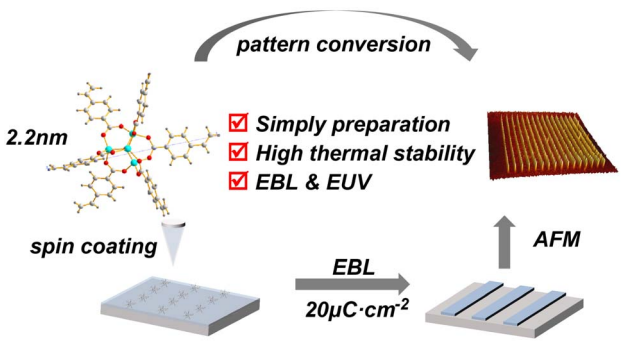

Scheme 1 Schematic illustration of Zn–VBA transfer from molecule to lithography patterning.

Results and discussion

Design and characterization

Due to the strong resonance towards EUV light of zinc, Zn-based clusters are expected to be promising patterning materials.[7,16,17] Previous reported zinc–oxo clusters mainly focused on the $[Zn_4O]^{6+}$ type materials by using aliphatic acid ligands to constitute the organic shell, and the lithographic performance of the materials has been studied in detail. However, to the best of our knowledge, developing functional aromatic acid-containing zinc–oxo clusters as EUV patterning materials have yet to be reported. Since the aromatic ring is electron-rich and more rigid than the aliphatic series, it was anticipated that the introduction of phenyl subunits into the cluster would render the molecule more rigid without precluding their ability to act as effective metal complexants to provide good thermal stability, solubility and film-formation ability.[28,29] Based on the above design criteria, 4-vinylbenzoic acid (**VBA**) was introduced as the organic ligand to construct the zinc–oxo cluster Zn–**VBA**. In addition, Zn–**BA** and Zn–**TBA** clusters containing benzoic acid (**BA**) and 4-trifluoromethyl benzoic acid (**TBA**) were also prepared as control molecules to study the electronic effects of *para*-substituted benzoic acids on the performance of zinc–oxo clusters (Fig. 1a, S1, and S2†). The electronic ESI† contains detailed synthetic procedures and characterization data of Zn–**VBA**, Zn–**BA** and Zn–**TBA** clusters.

Single-crystal X-ray diffraction analysis was performed to identify the structural properties of Zn–**VBA** (Fig. 1b and Table S1†) and Zn–**TBA** (Fig. S3 and Table S2†), while the crystal structure of Zn–**BA** from the reported literature was used.[30] Taking Zn–**VBA** as example, the crystal structure reveals that Zn–**VBA** comprises four Zn atoms bridged by one O atom (μ_4-O) and six 4-vinylbenzoic acid ligands. The central oxygen is bonded to four zinc atoms, and each zinc atom exhibits a tetrahedral geometry coordinated to the other three oxygen atoms from carboxylate groups of the peripheral ligands, with Zn–O bond distances of about 1.941(9) Å. The binding carboxylate groups from six 4-vinylbenzoic acid ligands to zinc atoms display C–O bond lengths of 1.255(6) to 1.264(8) Å, and bond angles of 124.7(6)°, indicating the delocalization of the π-electrons within the bridging bidentate ligands. The whole molecule presents a spatially symmetric octahedral structure with a size of 2.2 nm, with each ligand orthogonally directed to the inner inorganic core. Only weak intermolecular CH–π interactions are observed between the phenyl rings of adjacent

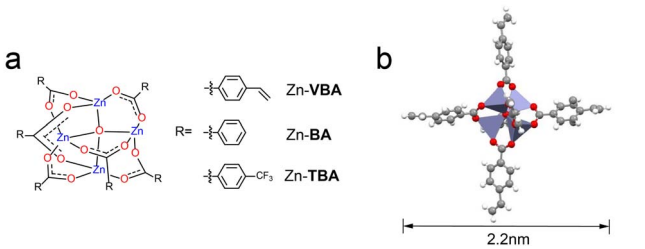

Fig. 1 (a) Chemical structures of zinc–oxo clusters and (b) crystal structure of Zn–VBA.

molecules, which inhibits compact molecular packing. Therefore, such organic–inorganic hybrid structural properties are expected to endow the zinc–oxo clusters with good solubility in spin-coating solvents, high sensitivity, and good thermal stability, all of which are crucial for the resolution targets in EUVL.

Thermal stability

Thermal stability is a key factor that determines the performance of photoresist materials during the baking steps, which is important for film formation, reactions using light irradiation, and final pattern quality.[31] Low thermal stability limits the application of photoresist materials in the photolithography process. Thermogravimetric analysis (TGA) was performed to investigate the thermal stability of the zinc–oxo clusters (Fig. 2). No obvious mass loss was observed at temperatures below 300 °C. The initial loss of 5 wt% for the three clusters occurred in the following order: Zn–**VBA**, 392 °C > Zn–**BA**, 327 °C > Zn–**TBA**, 326 °C. All of them exhibited much better thermal stability than the reported zinc–oxo clusters containing aliphatic acid ligands which showed T_{95} generally below 200 °C. Further increasing the temperature induced loss of organic ligands, which were completely decomposed at >500 °C and left the ZnO inner core. Moreover, the weight ratios of residues were determined to be 26.6%, 21.6%, and 30.4% for Zn–**VBA**, Zn–**TBA**, and Zn–**BA**, respectively, which corresponds to the calculated results.

The natural bond orbitals (NBO)[32] were calculated and analyzed (Table 1) to study the chemical bonding properties in

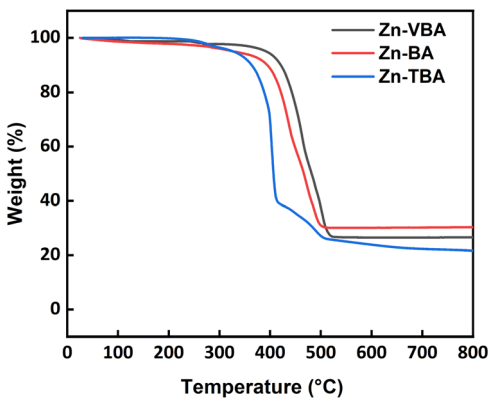

Fig. 2 Thermogravimetric analyses of as-synthesized zinc–oxo clusters.

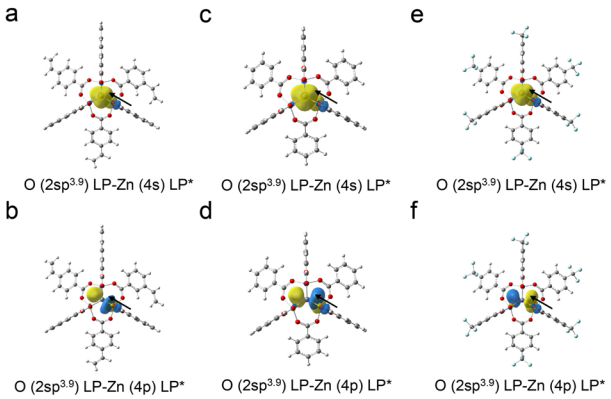

Fig. 3 Schematic contours of the electron transfer that occurs from the lone pair of O atom to the antibonding orbital of Zn atom based on the NBO analysis. (a) and (b) Zn–**VBA**. (c) and (d) Zn–**BA**. (e) and (f) Zn–**TBA**. The arrow indicates the direction of electron transfer.

the three clusters. It was revealed that Zn and outer O atoms are mainly bound by coordination bonds, whereas the others are bound by covalent bonds. Therefore, it can be assumed that the coordination bonds should be broken upon heating; that is, the thermal stability of the molecule depends on the stability of the coordination bond between Zn and O. The second-order perturbation stabilization energy $\Delta E(2)$ between the natural bond electron donor O atom and the electron acceptor Zn atom, which is used to evaluate their interaction intensities, was further analyzed. The larger the $\Delta E(2)$ value, the stronger the donor–acceptor interaction. Since the six peripheral ligands in the molecule have identical and symmetrical structures, only the analysis results of one of them are listed in Table 1. The schematic contours based on NBO analysis are shown in Fig. 3a–f.

Taking the Zn–**TBA** cluster as an example, the lone pair electrons of the approximate sp^3 hybrid orbital of O are found to be transferred to the unoccupied 4s and 4p orbitals of Zn. The total stabilization energy for second-order perturbation is calculated to be 50.1 kcal mol^{-1}. Similar coordination effects also exist in Zn–**BA** and Zn–**VBA** clusters. However, the stabilization energy for second-order perturbation is slightly higher than that of Zn–**TBA**, indicating stronger coordination effects. Because the O atom of the ligand participates in the π-conjugation of the benzene ring when a strong electron withdrawing group of CF_3 locates in its para position, as shown in Zn–**TBA**,

Table 1 Natural bond orbital analysis of molecules for bonding types and coordination properties

Compound	Donor NBO[a]	Occupancy	Acceptor NBO	Occupancy	$\Delta E(2)$ kcal mol^{-1}	
Zn–**TBA**	O ($2sp^{3.9}$) LP	1.931	Zn (4s) LP*	0.296	29.24	**50.1**[b]
	O ($2sp^{3.9}$) LP	1.931	Zn (4p) LP*	0.098	20.81	
Zn–**BA**	O ($2sp^{3.9}$) LP	1.838	Zn (4s) LP*	0.296	29.30	**52.3**
	O ($2sp^{3.9}$) LP	1.838	Zn (4p) LP*	0.121	23.01	
Zn–**VBA**	O ($2sp^{3.9}$) LP	1.838	Zn (4s) LP*	0.296	29.31	**55.9**
	O ($2sp^{3.9}$) LP	1.838	Zn (4p) LP*	0.121	26.56	

[a] NBO (natural bond orbital). [b] The bold data are the sum of $\Delta E(2)$.

the electron donating capability of O is reduced, and thus the coordination bond weakens. In contrast, the presence of a contraposition vinyl group enhanced the electron donating capability of O in Zn–**VBA**. According to the above calculation results, the strength of the Zn–O coordination bond in three molecules decreases in the following order: Zn–**VBA** > Zn–**BA** > Zn–**TBA**. This result is consistent with the experimental observations of TGA.

Solubility and film-forming ability

Solubility is crucial for the performance of photoresist materials in the film-forming and developing processes of lithography. The solubility of Zn–**VBA** was tested in solvents with different parameters, such as dispersion, polarity, and hydrogen-bonding capability. As shown in Table S3,† Zn–**VBA** has good solubility in common organic solvents such as acetone, cyclohexanone, ethyl lactate, toluene, PGMEA, and propylene glycol monomethyl ether. On the other hand, Zn–**VBA** is almost insoluble in *tert*-butanol, ethanol, diethylene glycol, and water.

The spin-coating method was then used to further study the film-forming ability of Zn–**VBA** in its "good" solvents, including PGMEA, cyclohexanone, and ethyl lactate. The morphology of the spin-coated films was initially evaluated by atomic force microscopy (AFM) (Fig. 4a–d and Table 2). Uniform films were formed at concentrations of 10–30 mg mL^{-1}, and the thickness was determined to be 30–40 nm (Fig. 4a–d). The roughness (Rq), an important parameter to evaluate the film quality, was quantified as 0.20, 0.28, 0.24, and 0.33 nm for the four conditions, indicating good film-forming properties in these solvents. Furthermore, although Zn–**VBA** showed good solubility and film formation in PGMEA (Fig. 4c), it was found that the Rq value increased when the concentration of Zn–**VBA** in PGMEA solution was increased from 20 to 30 mg mL^{-1}. High concentrations lead to the formation of precipitates, as reflected by the bright spot observed in the AFM image (Fig. 4d).

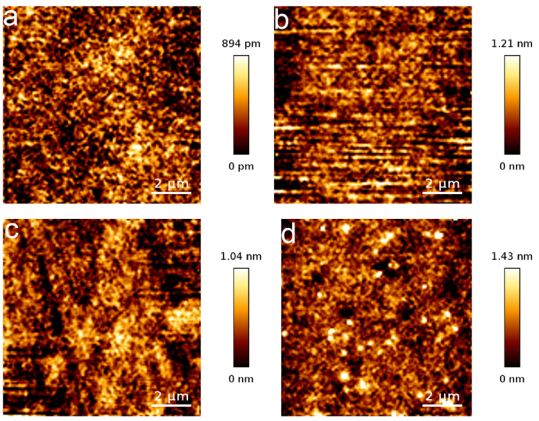

Fig. 4 AFM images of Zn–VBA under the film-formation conditions a–d shown in Table 2.

Storage stability

In general, polymer-based photoresist materials should be stored at optimal temperatures and protected from light illumination to avoid particle formation and photoactive compound loss, which would result in materials that were no longer capable of performing specific functions. The same requirements apply to inorganic–organic photoresist materials with particle features that tend to congregate into larger clusters. Such a conglomerate phenomenon is highly related to solvent properties. The storage stability of Zn–**VBA** was investigated in solvents such as cyclohexanone, ethyl lactate, and PGMEA. After one week of storage at 25 °C, a large number of insoluble substances precipitated in the ethyl lactate solution, whereas the other two solutions remained nearly transparent (Fig. S4†).

The electrostatic interactions between Zn–**VBA** and solvent molecules, such as cyclohexanone, ethyl lactate, PGMEA, and *tert*-butanol, were investigated to elucidate the influence of solute–solvent interactions on the storage stability of Zn–**VBA**. The electrostatic potential (ESP) of Zn–**VBA** (Fig. 5a and b) and different solvent molecules (Fig. 5c) were calculated. The red area is negative and indicates nucleophilicity; the blue area is positive and represents electrophilicity; and the green area is neutral.

The ESP results revealed that the inner inorganic core showed nucleophilic activity. However, the inner core was unable to contact solvent molecules. Unlike the inner core, the peripheral organic ligands showed neutral and weak electrophilicity. Regarding the various solvents, the ESP results indicated that =O in PGMEA and cyclohexanone showed nucleophilic behavior, while *tert*-butanol showed electrophilic behavior owing to the presence of –OH. Ethyl lactate, in particular, showed dual electrostatic interaction because of the uniqueness of its structure (containing both =O and –OH). In addition, the hydroxyl groups in the two solvent molecules can form intermolecular hydrogen bonds between the solvent molecules, which weakened the electrostatic interaction with Zn–**VBA** and caused the Zn–**VBA** to precipitate.

Table 2 Roughness (Rq) values under different conditions

Conditions	Solvent	Speed	Conc.	Rq	PAB[a]
a	Cyclohexanone	3000 rpm	30 mg mL^{-1}	0.20 nm	90 °C 60 s
b	Ethyl lactate	3000 rpm	30 mg mL^{-1}	0.28 nm	90 °C 60 s
c	PGMEA	3000 rpm	20 mg mL^{-1}	0.24 nm	90 °C 60 s
d	PGMEA	3000 rpm	30 mg mL^{-1}	0.33 nm	90 °C 60 s

[a] PAB (the parameter of post-application baking).

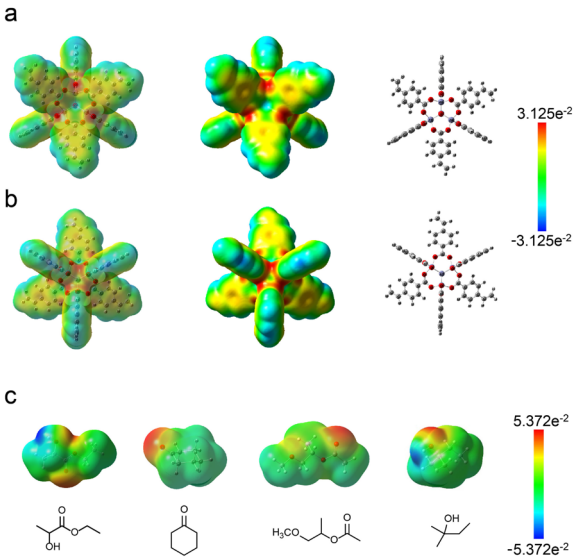

Fig. 5 Optimized geometric structure and the ESP contours of Zn–**VBA** and solvent molecules calculated using DFT method: (a) top view of Zn–**VBA**; (b) side view of Zn–**VBA**; and (c) ethyl lactate, cyclohexanone; PGMEA, and *tert*-butanol. (Colour band unit: per Hartree.).

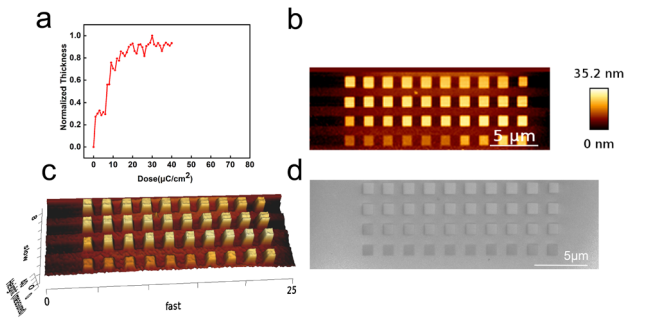

Fig. 6 (a) Sensitivity contrast curve of Zn–**VBA** resist at different exposure doses (1–40 μC cm^{-2}) and (b) top view, (c) oblique view of AFM image, and (d) FE-SEM image of Zn–**VBA** patterns.

During the dissolution process, the solvent molecules (cyclohexanone, PGMEA, and ethyl lactate containing =O) are in constant contact with the solute molecules, exhibiting a dynamic behavior under violent stirring. Thus, the Zn–**VBA** dissolves under the driving force of electrostatic interaction. However, owing to the strong hydrogen bonds formed between the solvent molecules in ethyl lactate, solute molecules (Zn–**VBA**) precipitated after standing for a while, whereas the cyclohexanone and PGMEA solutions are relatively stable. It is because of the presence of –OH in ethyl lactate, which makes =O a better hydrogen-bond acceptor. Hence, the broken hydrogen bonds were restored, as evidenced by the redissolution of Zn–**VBA** into ethyl lactate following heating or ultrasonic treatment. The electrostatic interaction also accounted for the poor solubility of Zn–**VBA** in *tert*-butanol owing to the presence of only –OH. Based on the dissolution and precipitation behaviours, the comparative storage stability of Zn–**VBA** in different solvents was as follows: cyclohexanone = PGMEA > ethyl lactate.

Lithography

Based on the above analysis of the structure–property relationship of the obtained zinc–oxo cluster (Zn–**VBA**), we investigated its potential as resists for EBL and EUVL. The energy absorption processes between EUVL and EBL are different; however, both techniques generate low-energy secondary electrons in photoresists through ionization, which are responsible for chemical reactions.[33–41] The detailed experimental setups of pre-expose preparation are provided in the ESI.†

To evaluate the sensitivity of the Zn–**VBA**, the normalized resist thickness curve was measured in the form of step exposure by EBL because it can produce high-energy electrons during radiation to induce chemical reactions for lithography patterning (Fig. 6a). The exposure dose was varied from 0.2× to 8.0× with an increment of 0.2× at the initial dose of 5 μC cm^{-2}, forming forty 1 μm square boxes on the silicon wafer because of the negative tone character of Zn–**VBA** photoresist (Fig. 6b–d). It was found that the contrast (γ) of Zn–**VBA** resist is 1.4. At the e-beam energy of 30 keV, the sensitivity was calculated to be 20 μC cm^{-2}, corresponding to the required energy to pattern the resist.[42]

The interaction between the beam cross section and the resist film demonstrated that the high-energy electron beam induced a large penetration depth into the substrate.[43] Thus, 30 keV electron beam was chosen instead of the usual 5 keV or 10 keV for EBL test. A field-emission scanning electron microscope (FE-SEM) was used for surface morphological analysis of high-resolution patterned samples at the doses of 5 μC cm^{-2} (Fig. S5a, b,† 7a and b) and 20 μC cm^{-2} (Fig. S5c, d,† 7e and f). To better present the topographical information of the Zn–**VBA** resist, FE-SEM images were measured by a 45° turntable rotation in the *Z*-axis direction, as shown in Fig. 7a, b, e and f. Exposure doses of 5 and 20 μC cm^{-2} produced the same 200 nm L/4S resolution; however, remaining at the dose of 20 μC cm^{-2}. The difference was clearly observed in the corresponding AFM images (Fig. 7c, d, g and h) and the section profiles of the AFM images (Fig. S6a and b†). Interestingly, the sensitivity of Zn–**VBA** is higher than that of most reported negative e-beam resists.

The ligands in the cluster largely determined the patterning properties. The patterning performance between Zn–**VBA** (with C=C) and Zn–**TBA** (without C=C) was evaluated by EBL to clarify the role of ligands during radiolysis (Fig. S7a and b†). The exposed patterns showed 100 nm L/2S resolution for both Zn–**VBA** and Zn–**TBA** with no bridging or buckling. However, the sensitivity of Zn–**VBA** (20 μC cm^{-2}) is an order of magnitude higher than that of Zn–**TBA** (550 μC cm^{-2}). Zn–**VBA** and Zn–**TBA** show different reaction mechanisms in the EBL test. Upon e-beam exposure, the zinc–oxo clusters are ionized, resulting in the emission of a photoelectron and the formation of a radical cation, which can further induce decarboxylation of the peripheral ligands. Then the resulting Zn-sites occur in oxidative/hydrolysis reaction and further aggregate with the neighboring clusters to form Zn–O analogs when the film is exposed to the ambient atmosphere after e-beam exposure. For

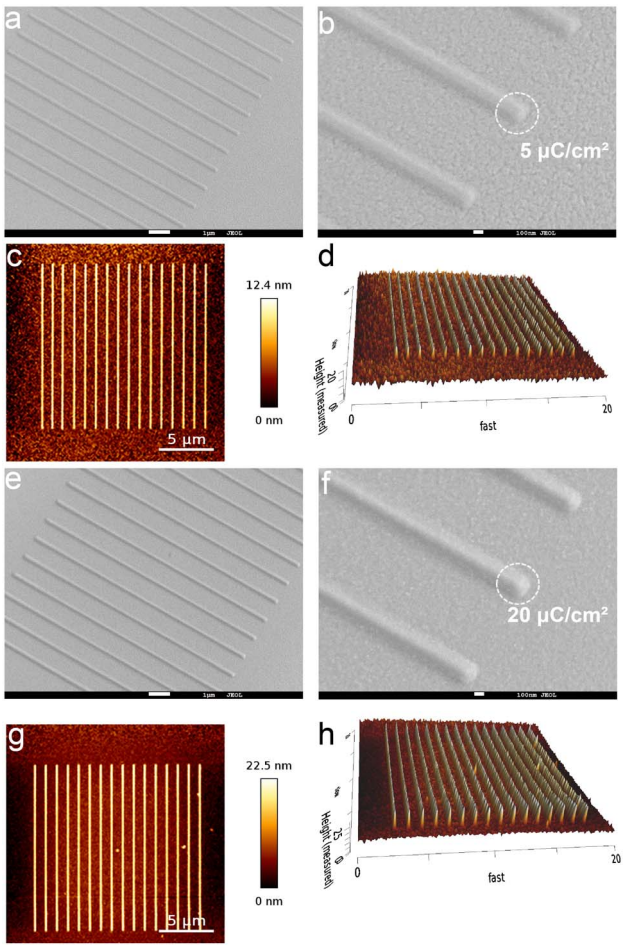

Fig. 7 FE-SEM images with (a) ×8500 and (b) ×40 000 magnification at the dose of 5 μC cm^{-2} and corresponding (c) top view and (d) oblique view of AFM images. FE-SEM images with (e) ×8500 and (f) ×40 000 magnification at the dose of 20 μC cm^{-2} and corresponding (g) top view and (h) oblique view of AFM images.

Zn–**VBA**, in addition to the decarboxylation reaction, it undergoes an extra reaction where the terminal double bonds in the 4-vinylbenzoic acid ligands are polymerized to form a network due to the presence of highly reactive radical to initiate the polymerization reaction.[27,44–48] This is the possible reason for the higher sensitivity of Zn–**VBA** than that of Zn–**TBA**. Because of the excellent e-beam performance of Zn–**VBA**, the lithographic performance under EUVL was further explored.

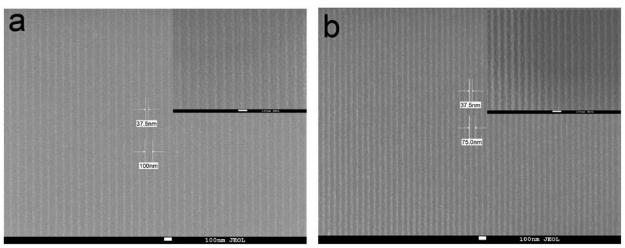

Fig. 8 Zn–VBA resist patterned by EUV lithography (92.5 mJ cm^{-2}) performed with different pitches: (a) 100 nm, (b) 75 nm.

The obtained Zn–**VBA** film was exposed to EUV and then developed with MIBK : IPA = 1 : 3. The FE-SEM images showed excellently dense patterns at 92.5 mJ cm^{-2} with 37.5 nm 3L/5S resolution and no bridging or residues in the unexposed areas (Fig. 8a). However, the patterns showed bridging or buckling for other pitches (Fig. 8b and S8†). These results indicate that the Zn–**VBA** resist exhibits great potential for application in EUV and can be a strong candidate for the next generation of photolithographic materials.

Conclusions

In this study, we presented a novel zinc–oxo cluster, Zn–**VBA**, which contains the $[Zn_4O]^{6+}$ as the inner core and six 4-vinylbenzoic acids as a component of the organic shell. Zn–**VBA** shows a size of 2.2 nm, meeting the high-resolution requirements for advanced lithography technology. It is proved that Zn–**VBA** solves the problem of low purity of zinc–oxo clusters used in photoresists while also being easy to synthesize with good batch stability. Zn–**VBA** also showed high thermal stability and good solubility in organic solvents such as cyclohexanone and PGMEA. Moreover, Zn–**VBA** was fabricated into a uniform thin film with extremely low roughness using the spin-coating method. The obtained Zn–**VBA** films performed well in the EBL and EUVL tests without additives, inspiring future exploration of MOCs resist materials for advanced lithography.

Conflicts of interest

The authors declare no competing financial interests.

Acknowledgements

This work was supported by the National Natural Science Foundation of China (NSFC, 21925802, 22090011, 22008024), the National Key Research and Development Plan (2018AAA0100301), Key R&D Program of Shandong Province (2021CXGC010308), and the Fundamental Research Funds for China Central Universities (DUT22LAB601 and DUT21ZD407).

Notes and references

1 J. Liu, H. Guo, M. Li, C. Zhang, Y. Chu, L. Che, Z. Zhang, R. Li, J. Sun and Y. Lu, *J. Mater. Chem. A*, 2021, **9**, 4262–4272.
2 Z.-S. Wu, K. Parvez, X. Feng and K. Müllen, *J. Mater. Chem. A*, 2014, **2**, 8288–8293.
3 F. Luo, L. J. Heyderman, H. H. Solak, T. Thomson and M. E. Best, *Appl. Phys. Lett.*, 2008, **92**, 102505.
4 A. Vaida, D. Christian, F. Patrick, A. G. Detlev, J. H. Laura, L. Feng, O. Sven, P. Celestino, S. Pratap, T. Tom, T. Audrey, D. Christian and H. S. Harun, *J. Micro/Nanolithogr., MEMS, MOEMS*, 2009, **8**, 021204.
5 Z. Wang, X. Yao, H. An, Y. Wang, J. Chen, S. Wang, X. Guo, T. Yu, Y. Zeng, G. Yang and Y. Li, *J. Microelectron. Manuf.*, 2021, **4**, 21040101.
6 X. Guo, G. Yang and Y. Li, *Laser Optoelectron. Prog.*, 2022, **59**, 0922004.

7 L. Li, X. Liu, S. Pal, S. Wang, C. K. Ober and E. P. Giannelis, *Chem. Soc. Rev.*, 2017, **46**, 4855–4866.
8 T. Rath, C. Padeste, M. Vockenhuber, C. Fradler, M. Edler, A. Reichmann, I. Letofsky-Papst, F. Hofer, Y. Ekinci and T. Griesser, *J. Mater. Chem. A*, 2013, **1**, 11135–11140.
9 S. Hu, J. Chen, T. Yu, Y. Zeng, X. Guo, S. Wang, G. Yang and Y. Li, *J. Photochem. Photobiol., A*, 2023, **436**, 114351.
10 S. Kawakami, T. Onitsuka, Y. A. Kamei, S. Shimura and C. Ha Park, *Proc. SPIE*, 2022, **12055**, 120550N.
11 S. Hu, J. Chen, T. Yu, Y. Zeng, S. Wang, X. Guo, G. Yang and Y. Li, *J. Mater. Chem. C*, 2022, **10**, 9858–9866.
12 Y. Wang, L. Chen, J. Yu, X. Guo, S. Wang and G. Yang, *R. Soc. Open Sci.*, 2021, **8**, 202132.
13 H.-T. Oh, K. Kim, B.-G. Park, S. Lee and J.-K. Lee, *Proc. SPIE*, 2020, **11326**, 113260B.
14 J. Chen, Q. Hao, S. Wang, S. Li, T. Yu, Y. Zeng, J. Zhao, S. Yang, Y. Wu, C. Xue, G. Yang and Y. Li, *ACS Appl. Polym. Mater.*, 2019, **1**, 526–534.
15 X. Peng, Y. Wang, J. Xu, H. Yuan, L. Wang, T. Zhang, X. Guo, S. Wang, Y. Li and G. Yang, *Macromol. Mater. Eng.*, 2018, **303**, 1700654.
16 H. Xu, K. Sakai, K. Kasahara, V. Kosma, K. Yang, H. C. Herbol, J. Odent, P. Clancy, E. P. Giannelis and C. K. Ober, *Chem. Mater.*, 2018, **30**, 4124–4133.
17 N. Thakur, L.-T. Tseng, M. Vockenhuber, Y. Ekinci and S. Castellanos, *J. Micro/Nanolithogr., MEMS, MOEMS*, 2019, **18**, 043504.
18 B. Cardineau, R. Del Re, M. Marnell, H. Al-Mashat, M. Vockenhuber, Y. Ekinci, C. Sarma, D. A. Freedman and R. L. Brainard, *Microelectron. Eng.*, 2014, **127**, 44–50.
19 D. Wang, X. Yi and L. Zhang, *Sci. China: Chem.*, 2022, **65**, 114–119.
20 X. Yi, D. Wang, F. Li, J. Zhang and L. Zhang, *Chem. Sci.*, 2021, **12**, 14414–14419.
21 Y. Ekinci, A. M. Brouwer, S. Castellanos, L. Wu, J. Haitjema and R. Fallica, *J. Micro/Nanolithogr., MEMS, MOEMS*, 2018, **17**, 023505.
22 N. Thakur, R. Bliem, I. Mochi, M. Vockenhuber, Y. Ekinci and S. Castellanos, *J. Mater. Chem. C*, 2020, **8**, 14499–14506.
23 N. Thakur, M. Vockenhuber, Y. Ekinci, B. Watts, A. Giglia, N. Mahne, S. Nannarone, S. Castellanos and A. M. Brouwer, *Proc. SPIE*, 2019, **10957**, 109570D.
24 A. Grebenko, A. Bubis, K. Motovilov, V. Dremov, E. Korostylev, I. Kindiak, F. S. Fedorov, S. Luchkin, Y. Zhuikova, A. Trofimenko, G. Filkov, G. Sviridov, A. Ivanov, J. T. Dull, R. Mozhchil, A. Ionov, V. Varlamov, B. P. Rand, V. Podzorov and A. G. Nasibulin, *Adv. Funct. Mater.*, 2021, **31**, 2101533.
25 J. Gonzalez-Estrella, J. A. Field, C. K. Ober and R. Sierra-Alvarez, *Green Mater.*, 2019, **7**, 109–117.
26 S. M. Lewis, M. S. Hunt, G. A. DeRose, H. R. Alty, J. Li, A. Wertheim, L. De Rose, G. A. Timco, A. Scherer, S. G. Yeates and R. E. P. Winpenny, *Nano Lett.*, 2019, **19**, 6043–6048.
27 R. Kumar, M. Chauhan, M. G. Moinuddin, S. K. Sharma and K. E. Gonsalves, *ACS Appl. Mater. Interfaces*, 2020, **12**, 19616–19624.
28 K. E. Riley and P. Hobza, *Acc. Chem. Res.*, 2013, **46**, 927–936.
29 P. Jena and Q. Sun, *Chem. Rev.*, 2018, **118**, 5755–5870.
30 J. Lewinski, W. Bury, M. Dutkiewicz, M. Maurin, I. Justyniak and J. Lipkowski, *Angew. Chem., Int. Ed.*, 2008, **47**, 573–576.
31 W.-A. C. Bauer, C. Neuber, C. K. Ober and H.-W. Schmidt, *Adv. Mater.*, 2011, **23**, 5404–5408.
32 A. E. Reed, L. A. Curtiss and F. Weinhold, *Chem. Rev.*, 1988, **88**, 899–926.
33 E. D. Martinez, A. Prado, M. Gonzalez, S. Anguiano, L. Tosi, L. Salazar Alarcon and H. Pastoriza, *Front. Mater.*, 2021, **8**, 629792.
34 K.-d. Seong, J.-Y. Jung, J. Kang, D.-S. Kim, L. Lyu, S. Seo, J.-H. Kim and Y. Piao, *J. Mater. Chem. A*, 2020, **8**, 25986–25994.
35 N. R. Kiran, M. Chauhan, S. K. Sharma, S. Ghosh and K. E. Gonsalves, *ACS Appl. Electron. Mater.*, 2020, **2**, 3805–3817.
36 A. S. Gangnaik, Y. M. Georgiev and J. D. Holmes, *Chem. Mater.*, 2017, **29**, 1898–1917.
37 S. Ghosh, C. P. Pradeep, S. K. Sharma, P. G. Reddy, S. P. Pal and K. E. Gonsalves, *RSC Adv.*, 2016, **6**, 74462–74481.
38 L. Li, H. Lu and K. Deng, *J. Mater. Chem. A*, 2013, **1**, 2089–2093.
39 Y. Chen, *Microelectron. Eng.*, 2015, **135**, 57–72.
40 M. Tu, B. Xia, D. E. Kravchenko, M. L. Tietze, A. J. Cruz, I. Stassen, T. Hauffman, J. Teyssandier, S. De Feyter, Z. Wang, R. A. Fischer, B. Marmiroli, H. Amenitsch, A. Torvisco, M. d. J. Velasquez-Hernandez, P. Falcaro and R. Ameloot, *Nat. Mater.*, 2021, **20**, 93–99.
41 Y. Miao, D. T. Lee, M. D. de Mello, M. Ahmad, M. K. Abdel-Rahman, P. M. Eckhert, J. A. Boscoboinik, D. H. Fairbrother and M. Tsapatsis, *Nat. Commun.*, 2022, **13**, 420.
42 M. Yogesh, M. G. Moinuddin, M. Chauhan, S. K. Sharma, S. Ghosh and K. E. Gonsalves, *ACS Appl. Electron. Mater.*, 2021, **3**, 1996–2004.
43 Z. Cui, *Nanofabrication: Principles, Capabilities and Limits*, Springer, New York, 2008.
44 S. K. Sharma, R. Kumar, M. Chauhan, M. G. Moinuddin, J. Peter, S. Ghosh, C. P. Pradeep and K. E. Gonsalves, *Proc. SPIE*, 2020, **11326**, 1132604.
45 S. K. Sharma, M. Chauhan, R. Kumar, K. Palit, S. Choudhary, K. E. Gonsalves, D. Guerrero and D. P. Sanders, *Proc. SPIE*, 2021, **11612**, 1161208.
46 L. Wu, I. Bespalov, K. Witte, O. Lugier, J. Haitjema, M. Vockenhuber, Y. Ekinci, B. Watts, A. M. Brouwer and S. Castellanos, *J. Mater. Chem. C*, 2020, **8**, 14757–14765.
47 M. E. Krysak, J. M. Blackwell, S. E. Putna, M. J. Leeson, T. R. Younkin, S. Harlson, K. Frasure, F. Gstrein and S. Jose, *Proc. SPIE*, 2014, **9048**, 904805.
48 J. Passarelli, M. Murphy, R. Del Re, M. Sortland, L. Dousharm, M. Vockenhuber, Y. Ekinci, M. Neisser, D. A. Freedman and R. L. Brainard, *Proc. SPIE*, 2015, **9425**, 94250T.